

RESEARCH ARTICLE

NEUROSCIENCE

Dynamic compartmental computations in tuft dendrites of layer 5 neurons during motor behavior

Yara Otor^{1†}, Shay Achvat^{1†}, Nathan Cermak¹, Hadas Benisty², Maisan Abboud¹, Omri Barak¹, Yitzhak Schiller¹, Alon Poleg-Polsky^{3*}, Jackie Schiller^{1*}

Tuft dendrites of layer 5 pyramidal neurons form specialized compartments important for motor learning and performance, yet their computational capabilities remain unclear. Structural-functional mapping of the tuft tree from the motor cortex during motor tasks revealed two morphologically distinct populations of layer 5 pyramidal tract neurons (PTNs) that exhibit specific tuft computational properties. Early bifurcating and large nexus PTNs showed marked tuft functional compartmentalization, representing different motor variable combinations within and between their two tuft hemi-trees. By contrast, late bifurcating and smaller nexus PTNs showed synchronous tuft activation. Dendritic structure and dynamic recruitment of the *N*-methyl-D-aspartate (NMDA)-spiking mechanism explained the differential compartmentalization patterns. Our findings support a morphologically dependent framework for motor computations, in which independent amplification units can be combinatorically recruited to represent different motor sequences within the same tree.

Cortical pyramidal neurons (PNs) typically possess an elaborate dendritic tree, which serves to receive and integrate the vast synaptic inputs arriving to the neuron. In vitro and modeling studies have established the role of passive, active, and morphological properties of the dendritic tree in information processing. Especially important are local dendritic *N*-methyl-D-aspartate (NMDA) and calcium spikes, which endow PNs with the capability of performing multicompartmental parallel nonlinear computations, potentially increasing the computational power and storage capacity of PNs and ultimately of the network (1–5).

In vivo evidence for local representation of information in different tuft dendrites of layer 5 PNs is scarce (6, 7). Most reports show that the vast majority of calcium signals are highly correlated between different tuft branches, apical dendrites, and soma of same neurons (8–13), suggesting that the tuft and apical branches function mostly as a single compartment (14, 15). Thus, current literature presents a puzzling gap between the powerful computational capabilities of these dendrites, as suggested by in vitro and modeling studies (1, 16–22), and the much simpler computational scheme emerging from in vivo experiments.

In most in vivo studies, little consideration is given to the anatomical apical tuft structure

of the layer 5 PNs. Layer 5 PNs are composed of two main anatomical subtypes that differ in their dendritic apical morphology: thick-tufted pyramidal tract (PT) and slender-tufted intra-telencephalic (IT) neurons (23–30). Thick-tufted PTNs are further subdivided into two distinct subtypes on the basis of their nexus morphology and molecular markers (23, 24, 26, 31, 32). Because the degree of compartmentalization and electrical coupling is strongly dependent on the dendritic morphology (19, 33), we set out to examine motor representation in tuft dendrites of these two morphological types of thick-tufted layer 5 PTNs (24, 26) in the primary motor cortex (M1) (28–30). We developed a comprehensive experimental and analysis platform to reveal the relationships between the detailed structural pattern and the behaviorally related calcium activity.

Results

We imaged the activity of tuft dendrites from single thick-tufted layer 5 PTNs in M1 forelimb cortex using two-photon calcium imaging during two head-fixed behavioral paradigms: a hand reach and grab for a food pellet (34) and running on treadmill tasks (35) (Fig. 1, A and B). We used the sparse labeling method of adeno-associated virus (AAV) viral vectors encoding two fluorescent proteins: GCaMP6 for recording the activity (36) and mRuby2 for reconstructing the morphology of the tree (Fig. 1, C to F) with a high degree of certainty. This resulted in the transfection of only a few layer 5 PTNs in our field of view (Fig. 1E; see materials and methods) and enabled us to trace tuft dendrites to their parent soma with high accuracy. Overall, we recorded 28 thick-

tufted layer 5 PTNs in 22 mice. We first reconstructed the dendritic morphology from the two-photon volumetric Z-stack (Fig. 1C). We then used single-plane calcium imaging (30-Hz frame rate) to simultaneously record the activity of multiple dendritic tuft regions of interest (ROIs) of the same neuron (Fig. 1, E and F; on average, for each tree we sampled from 80.4 ± 11% of the terminal branches). These ROIs were aligned to the anatomical tree structure using custom software (see materials and methods).

Thick-tufted layer 5 PTNs are divided into two main well-established subtypes on the basis of their apical dendritic morphology with early and late bifurcating apical trunk (24, 26, 27). We used hierarchical clustering to subdivide our thick-tufted layer 5 PTNs on the basis of five morphological features (Fig. 1G and fig. S1, A to E). Consistent with previous studies, the clustering yielded two main subclasses: type 1, with early bifurcating apical tuft and long nexus, and type 2, with late bifurcating apical tuft and shorter nexus (Fig. 1G and fig. S1, F to H). Retrograde viral tracing of PTNs projecting to the medulla or cervical spinal cord revealed that M1 corticospinal PTNs yield a high proportion of type 1 dendritic morphology (fig. S1, I and J; 10 out of 11 of neurons in four mice were classified as type 1 neurons).

The two PTN subtypes demonstrated clear differences in their tuft calcium signals recorded during motor task performance. This was already apparent in the raw calcium imaging traces of individual trials (Fig. 1H, fig. S2, and movies S1 to S6). Type 1 thick-tufted layer 5 PTNs showed pronounced independent activity across their dendritic tuft branches (Fig. 1H and fig. S2), both in branches belonging to their right or left (R/L) tuft hemi-trees (Fig. 1H and fig. S2; division to left and right hemi-trees defined as all descendants of the first bifurcation branches) and within the hemi-trees (Fig. 1H). By contrast, type 2 PTNs did not show hemi-tree compartmentalization but did show more uniform dendritic tuft activation across their entire tuft tree (Fig. 1H and fig. S2).

To quantitatively investigate the correlations between the detailed tuft tree structure and dendritic activity in type 1 and 2 PTNs, we constructed and compared ROI distance matrices on the basis of dendritic structure and calcium activity. We obtained a structural distance matrix of the tuft tree by measuring the shortest path distance between all pairwise combinations of ROI locations, organized according to the tree structure (Fig. II). Calcium activity was extracted by identifying the calcium events in each ROI for all trials with the modified event detector ML SPIKE (37) (materials and methods and fig. S3A).

Calcium event amplitudes exhibited a long-tailed asymmetrical distribution (Fig. 1J and

¹Department of Physiology, Technion Medical School, Bat-Galim, Haifa 31096, Israel. ²Yale University School of Medicine; Bethany, CT, USA. ³Department of Physiology and Biophysics; University of Colorado School of Medicine, 12800 East 19th Avenue MS8307, Aurora, CO 8004, USA.

*Corresponding author. Email: jackie@technion.ac.il (J.S.); alon.poleg-polsky@cuanschutz.edu (A.P.-P.)

†These authors contributed equally to this work.

Fig. 1. M1 contains two populations of thick-tufted layer-5 PTNs with distinct morphologies and functional properties. (A) (Top) Behavioral setup for hand reach task. (Bottom) An ethogram and histogram annotating the behavior of an expert mouse. (B) (Top) Behavioral setup of head-fixed mice running on a treadmill. (Bottom) Example of velocity (cm/s) over time (s). (C and D) Z-stack of a single PTN acquired *in vivo* and its three-dimensional anatomical reconstruction.

(E) Single-imaging plane of a GCaMP6s-positive layer 5 PTN's tuft dendrites. ROIs are marked in yellow. (F) Schematics of the tuft morphology; dots represent ROIs. Same neuron in (C) to (F). (G) (Top) Hierarchical clustering of thick-tufted layer 5 PTNs based on five morphological parameters. (Bottom) Three example apical morphologies from each PTN type. Basal and oblique dendrites are not shown. Red numbers indicate the corresponding neurons in the clustering. (H) Calcium events ($\Delta F/F$ heat map) in single trials from the same three type 1 (left) and type 2 (right) PTNs shown in (G), arranged by the tree structure as indicated by the dendrogram. (I) Illustration of structure-activity correlations. Schematic representation of a layer 5 PTN with structural distance matrix presented as a heat map of the shortest path distance between each two ROIs (left) and illustrated activity traces for ROIs (right upper panel, dashed rectangles mark events belonging to different event clusters) and activity matrix showing Pearson correlation between ROI pairs presented for all events and for each event cluster (right lower panel). (J) (Left) Normalized calcium events histogram from 21 neurons for type 1 (black) and type 2 (gray) PTNs. (Right) Event distribution color coded by event cluster type for individual sessions in multiple neurons.

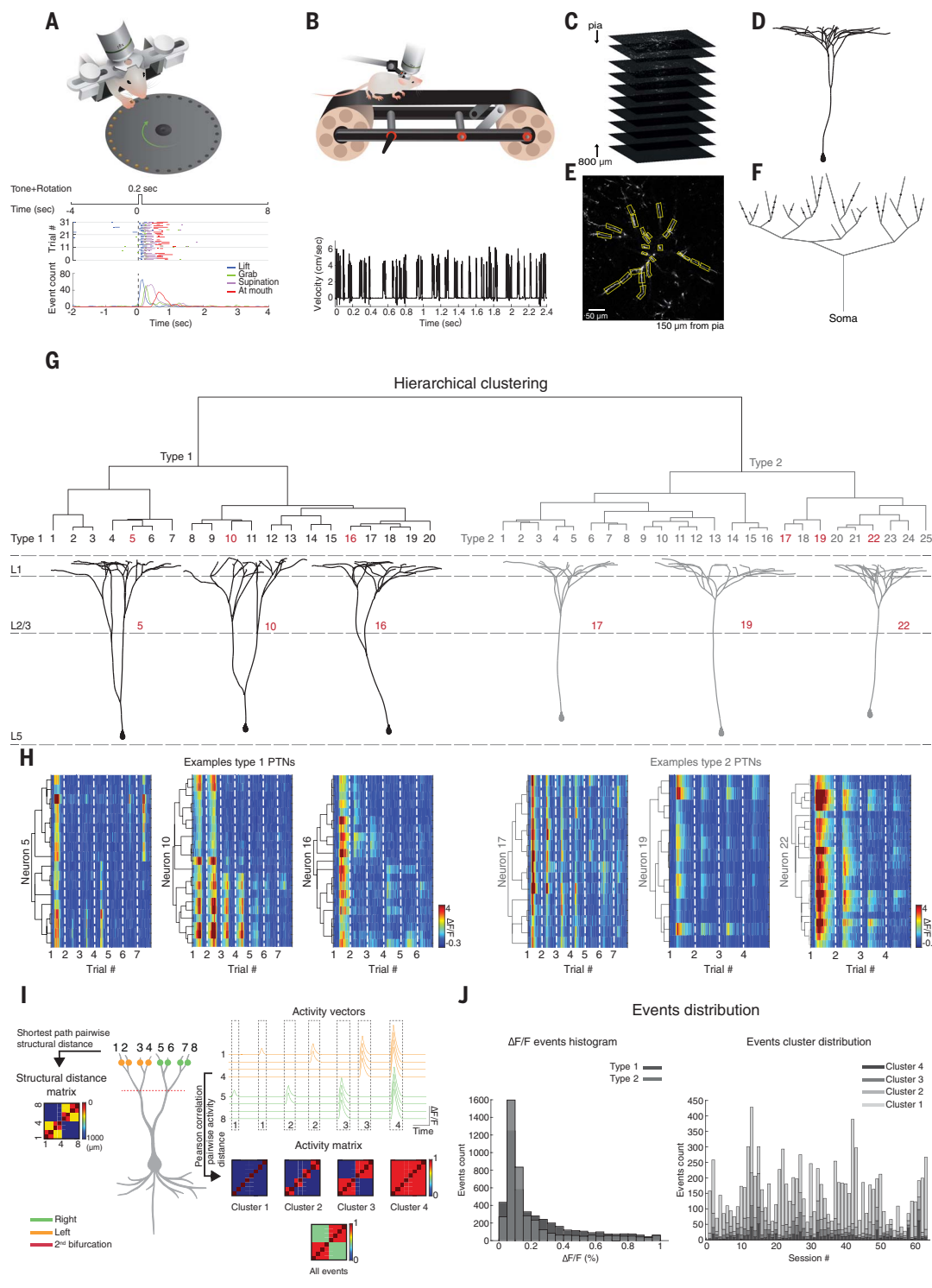


Fig. 2A). This raised the possibility of multiple subpopulations of calcium events. Indeed, visual inspection suggested four qualitatively distinct types of activation patterns in type 1 PTNs (single branch, subtree, hemi-tree, whole tree; Fig. 1, H and I; Fig. 2B; and fig. S2). To perform quantitative analysis of these differ-

ent event types, we subdivided the events into four clusters according to either their average amplitudes over all ROIs (see materials and methods) or the number of activated ROIs during each event (spatial activation extent) using the k-means algorithm (average percentage of events in cluster 1 = 66%, cluster 2 =

17%, cluster 3 = 10%, cluster 4 = 8% of the events; Fig. 1H, Fig. 2B, and figs. S2 and S3). With the calcium activity vectors and the structural distance matrix at hand, we constructed a pairwise Pearson correlation activity matrix arranged according to the structural distance matrix for each of the

Fig. 2. Compartmentalized activity in tuft dendrites of type 1 thick-tufted layer 5 PTNs during running on treadmill and hand reach.

(A) Calcium events histogram from one type 1 PTN during treadmill session. Arrows indicate values separating the four different event clusters.

(B) Examples of calcium events ($\Delta F/F$ heatmap) from the four event clusters in type 1 PTN. ROIs are arranged by the tree structure as indicated by the dendrogram, shown on the left (R, green; L, orange). (C) Two-dimensional tree diagram (left) and the corresponding structural distance matrix and dendrogram (right) of a type 1 PTN. Dots represent recorded ROIs.

(D) Two-dimensional PCA embedding of all ROIs activity; each dot represents a single ROI. (E) (Top) Matrices showing pairwise Pearson correlation coefficients computed from the calcium signals arranged by the tree structure shown in (C). (Bottom) Pearson correlation values as a function of shortest path distance fitted with a linear regression model. [(A) to (E)] Same neuron and session. ROIs compared within left hemi-tree (orange); within right hemi-tree (green) and between R/L hemi-trees (red). Black line represents linear regression model fit.

(F to H) As in (C) to (E) for a different type 1 PTN during a hand reach session. (I to M) Box plots of the following parameters: Mantel statistics comparing Pearson correlation and structural distance matrices (I), R^2 of linear regression model that predicted Pearson correlations

by distance (J), slope of linear regression model that predicted Pearson correlations by distance (K), R^2 of linear regression model that predicted Pearson correlations by distance calculated for the hemi-trees separately (L), and Z-score of the experimental Pearson correlations of within compared to between hemi-trees (mean Pearson_{within} – mean Pearson_{between}) calculated in relation to the shuffled distribution (M). * $p < 0.05$, ** $p < 0.01$, *** $p < 0.001$; blue asterisk, mean value. One-way analysis of variance (ANOVA) with Tukey post-hoc test (12 neurons, 8 animals, 27 sessions).

four calcium event clusters and for all events (Fig. 1, I and J).

We quantified the anatomical-functional correlations using three measures: First, we

performed principal component analysis (PCA) to embed the activity of each ROI across time and trials into a two-dimensional space of the two leading components that explain 84.42 ±

9.67% of the variance. Second, we used a Mantel test (38–40), which quantifies the degree of correlation between the functional activity and structural distance matrices. Third, we

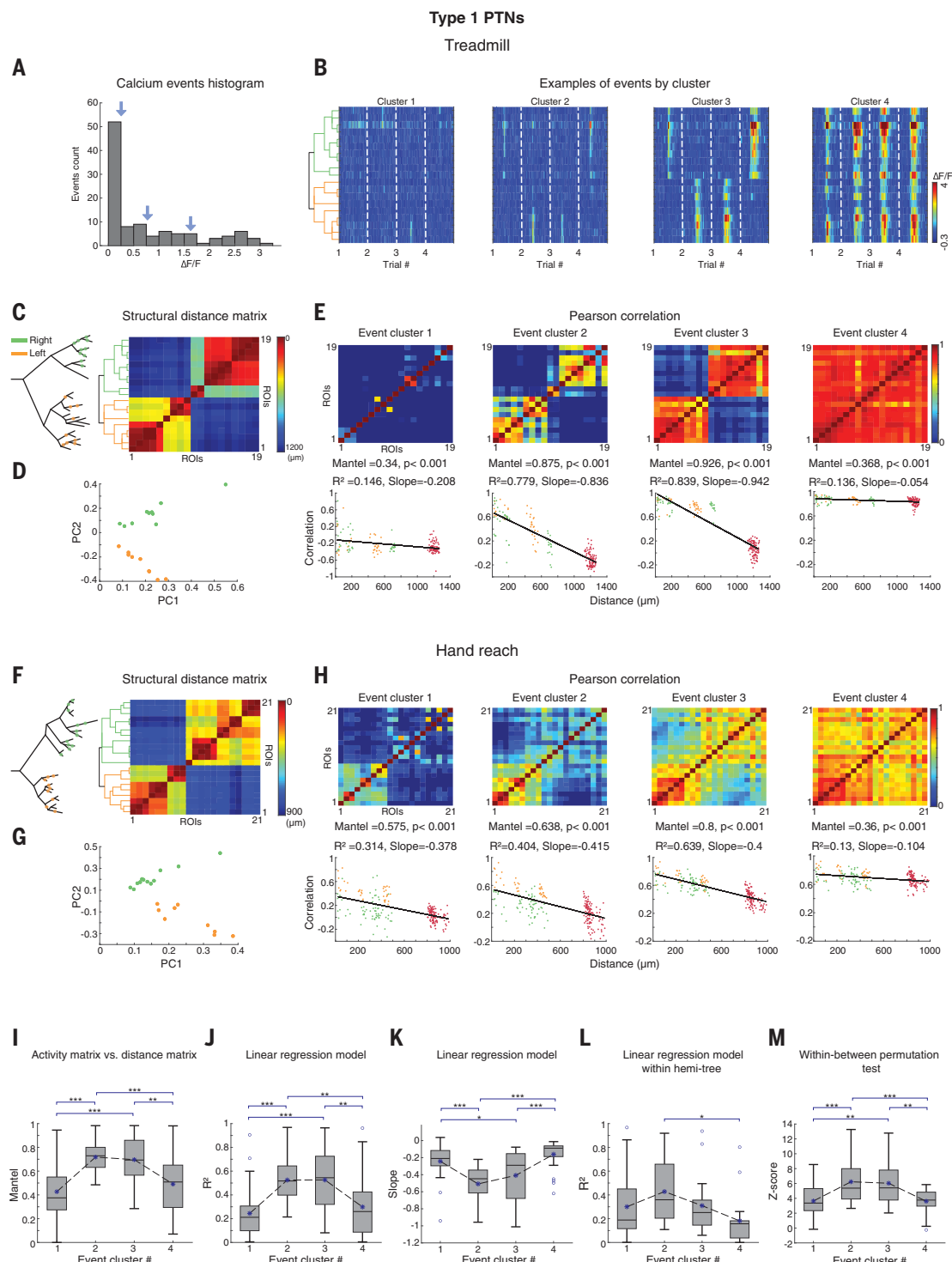
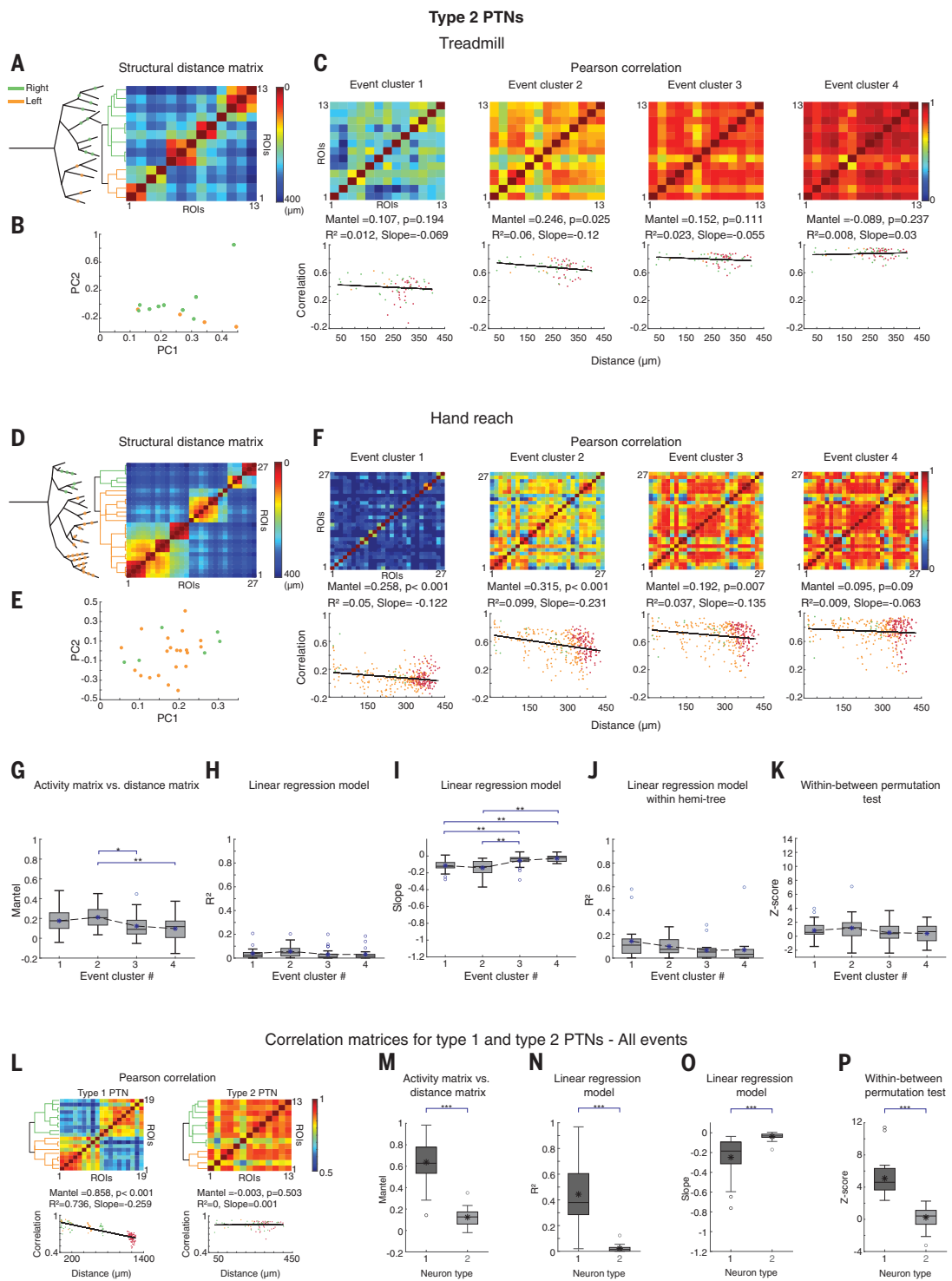


Fig. 3. Homogeneous activity in tuft dendrites of type 2 thick-tufted layer 5 PTNs during running on treadmill and hand reach. (A to K) As in (C) to (M) of Fig. 2 for type 2 PTNs. $*p < 0.05$, $**p < 0.01$, $***p < 0.001$; blue asterisk, mean value. One-way ANOVA with Tukey post-hoc test (9 neurons, 9 animals, 25 sessions). (L) Pairwise Pearson correlation coefficient matrices computed for all calcium events for type 1 (left) and type 2 (right) PTNs. (Bottom) Pearson correlation values as a function of shortest path distance fitted with a linear regression model for all events calculated for type 1 (left) and type 2 (right) PTNs. Type 1 PTN as in Fig. 2, C to E, and type 2 as in (A) to (C). (M to P) Box plots are the same as in (G) to (I) and (K) when all calcium events are considered for type 1 and type 2 PTNs.



measured the relationship between the pairwise Pearson activity correlations to the distance between ROIs with a linear regression (Fig. 2, C to H).

We first concentrated on type 1 PTNs. We observed strong compartmentalization of the tuft tree with a significant correlation between the tree structure and calcium activity during both motor tasks: hand reach and running on

treadmill. The first cluster, with the smallest calcium event amplitudes, typically involved correlated activity of individual or sister branches (Fig. 2, E and H). For this cluster, the Mantel statistics were relatively low (Fig. 2I), as was the linear correlation between the Pearson values and dendritic distance (Fig. 2, J to L, and fig. S4A; linear regression permutation test). For events with intermediate am-

plitudes corresponding to clusters 2 and 3, we observed high correlation between the activity and the tree structure, with strong compartmentalization of the tuft tree, ranging from correlated activity mapped to secondary and tertiary branches (event cluster 2; Fig. 2, C to H) or entire hemi-trees (event cluster 3; Fig. 2, C to H). The strong correlation between the anatomical and activity matrices in these

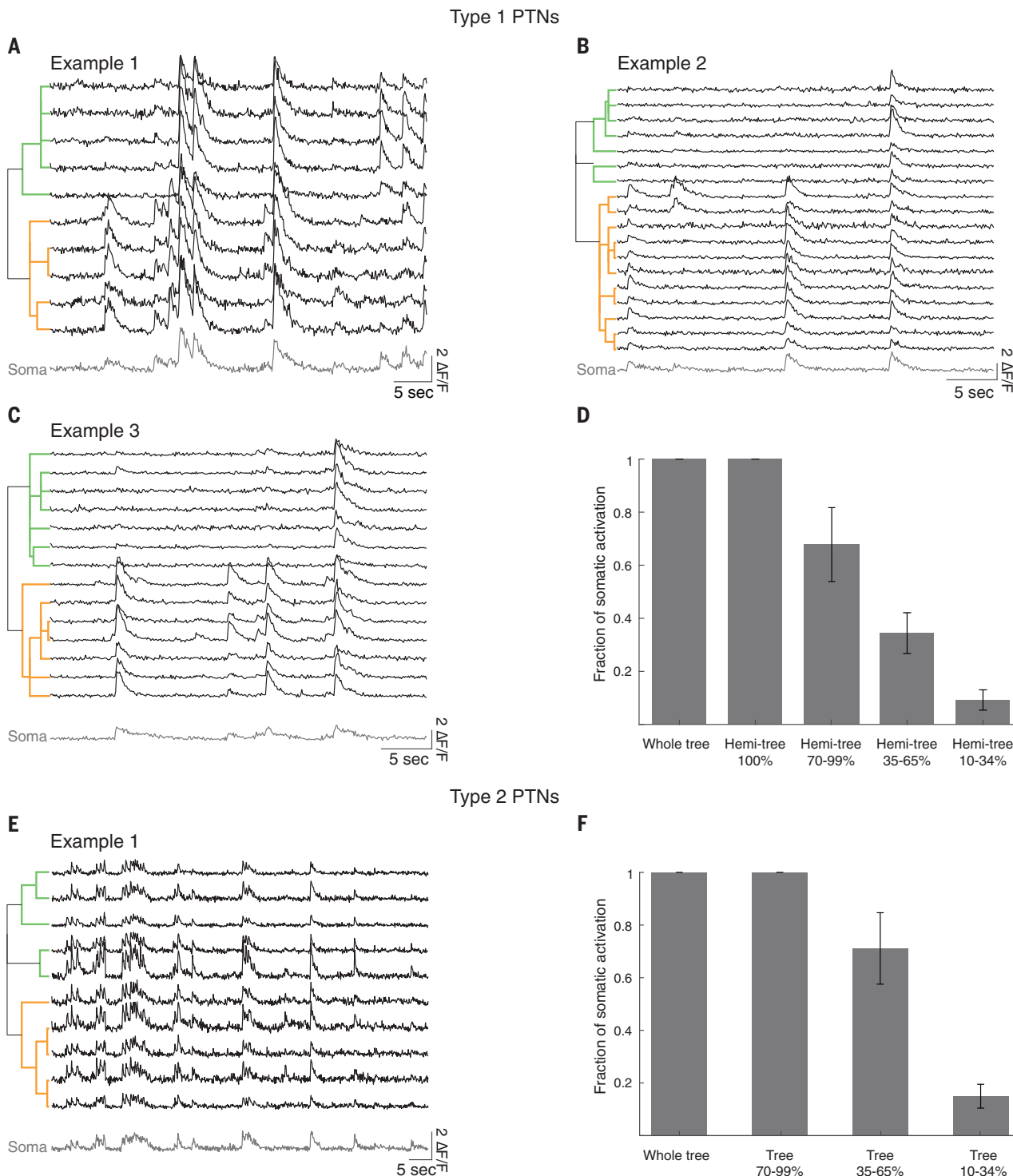


Fig. 4. Tuft and soma activity correlations. Quasi-simultaneous tuft and soma recordings were performed with an electrically tunable lens (ETL) (~10 Hz) in type 1 and 2 PTNs. (A to C) Examples of representative $\Delta F/F$ traces in the tuft and soma from a type 1 PTN (ROIs are arranged by the tree structure as indicated

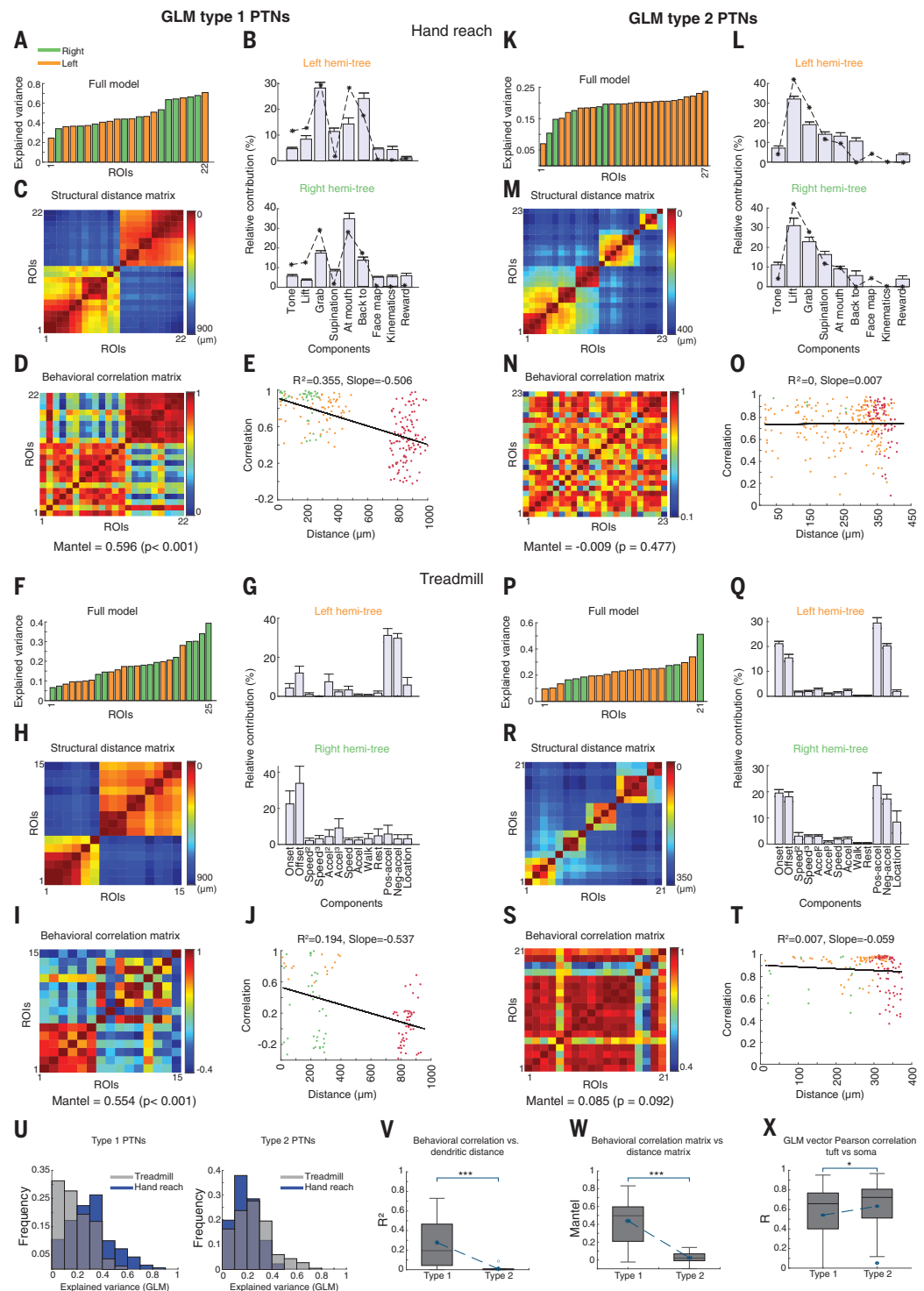
by the dendrogram). (D) Mean (\pm SD) fraction of tuft events that were simultaneously active with the soma for type 1 PTNs (seven neurons, six animals). (E) As in (A) for a type 2 PTN. (F) As in (D) for type 2 PTNs (three neurons, three animals).

clusters resulted in higher Mantel statistics (Fig. 2I) and a stronger dependence between pairwise Pearson correlation values and tuft dendritic distance (Fig. 2, E, H, and J to L, and fig. S4A; linear regression permutation test).

Finally, for the largest-amplitude calcium events (cluster 4), the activity was spread throughout the entire tuft tree, and responses in all ROIs were highly correlated (Fig. 2, E and H). This was manifested as lower Mantel

statistics (Fig. 2I) and lower dependence of the pairwise Pearson correlation values on dendritic distance (Fig. 2, E, H, and J to L, and fig. S4A; linear regression permutation test). Even in cluster 4 events, it is evident that some

Fig. 5. Modeling the contribution of the behavioral predictors to calcium activity of type 1 and type 2 PTNs using a generalized linear model (GLM). (A) Goodness of fit (R^2) of GLM full model for each ROI from a type 1 PTN during a hand reach session. (B) Mean relative contribution of modeled ROIs ($R^2 > 15\%$) for each of the behavioral predictors for right and left hemi-trees. Black asterisks on both graphs indicate values computed from somatic recordings of same neuron. (C) Structural distance matrix. ROIs with $R^2 < 0.15$ were excluded. (D) Pairwise Pearson correlation between the GLM relative contribution vectors for all included ROI pairs, arranged by the tree structure. (E) Pearson correlation values shown in (D) as a function of shortest path distance fitted with a linear regression model. (F to J) As in (A) to (E) during running on a treadmill. Same neuron in (A) to (J). (K to T) As in (A) to (J) for an example type 2 PTN. (U) (Left) Frequency of ROI's R^2 values of GLM full model for type 1 PTNs (10 animals, 14 neurons, 31 sessions). (Right) As in left panel for type 2 PTNs (9 animals, 10 neurons, 31 sessions). (V to X) Box plots of the following parameters: R^2 linear regression model that predicted the Pearson correlations of GLM relative contribution vector by dendritic distance (V), Mantel statistics comparing the structural distance matrix and the behavioral-correlation matrix (W), Pearson correlation between the soma's behavioral relative contributions and those of the tuft, for type 1 and type 2 PTNs (seven and four neurons, respectively) (X). *** $p < 0.001$; blue asterisks, mean value. Wilcoxon rank test.



portions of the tree were more strongly correlated than others. Similar results were obtained when event clustering was based on the spatial extent of calcium signals instead of their averaged amplitude (fig. S5).

To further examine the R/L hemi-tree segregation, we used two additional analysis methods: First, we shuffled the “within” and “between” tagging of ROI Pearson corre-

lation pairs while maintaining their pairwise correlation coefficient values. We found the experimental values of the difference between the mean Pearson correlations of within compared to between hemi-trees to be significantly higher compared to the shuffled distribution for all cluster events (Fig. 2M and fig. S6, A and C; Z-score >3.6). Second, we calculated the proportion of the variance explained (R^2) of

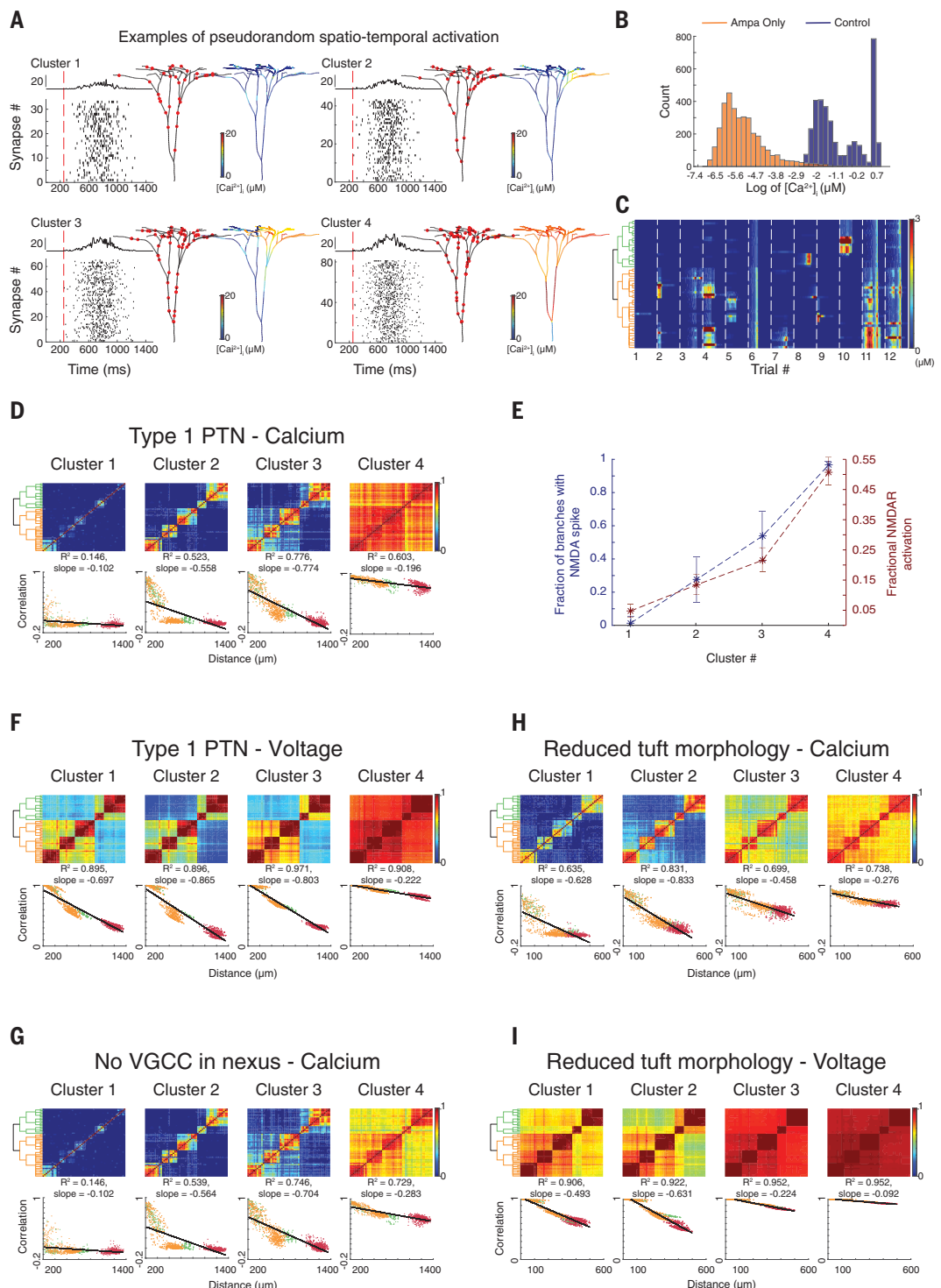
the calcium activity of each ROI in one hemi-tree by the activity of all ROIs in the contralateral hemi-tree using a linear regression model. The results further indicated compartmentalization of activity in the hemi-trees in clusters 1 to 3 (fig. S7A).

To facilitate the comparison between type 1 and type 2 PTNs, we also divided the events of type 2 PTNs into four clusters. The distributions

Fig. 6. Simulation of type 1 PTN explains in vivo activity by apical morphology and NMDA spikes.

(A) Examples of the temporal distribution of simulated pseudorandom synaptic activation patterns for the four event clusters in one trial. Top trace, the total number of activated synapses over time. (Right) The corresponding spatial input distribution and post-synaptic calcium signal (shown on a logarithmic scale). The average number of recruited synapses for each event cluster was 34 ± 13 , 48 ± 13 , 60 ± 15 , and 84 ± 29 .

(B) The distribution of the simulated evoked calcium events in the tuft dendrites of the reconstructed type 1 PTN. (C) Representative calcium activity in different simulation trials, arranged by the tree structure as indicated by the dendrogram, left. (D) (Top) Pairwise Pearson correlation coefficients computed from the tuft calcium signals arranged by the tree structure. (Bottom) Pearson correlation values as a function of shortest path distance fitted with a linear regression model (black). (E) The normalized number of tuft dendrites with NMDA spikes (blue) and the fractional NMDAR conductance (brown) for all event clusters. Error bars: SD. (F) As in (D), for tuft voltage correlations. (G) As in (D), in the absence of VGCC in the nexus. (H) As in (D), when the morphology of the tuft was reduced to match the extent of the tuft dendrites in type 2 PTNs shown in fig. S13A. (I) As in (H), for tuft voltage correlations. Color coding: orange and green represent data from the left and right hemi-trees, respectively. Red, comparison between R/L hemi-trees. Simulations for this figure are for the neuron in Fig. 2, C to E.



of peak calcium events and the peak calcium amplitudes of the clusters were comparable in type 1 and 2 PTNs (fig. S3, C and D). Type 2 PTNs did not show significant correlations between their tree structure and functional calcium activity for any of the calcium event clusters (Fig. 3 and figs. S4B and S7, B to E), and compartmentalization between their R/L hemi-tree was low (figs. S6, B and C, and S7A).

Thus, for type 2 PTNs except cluster 1, calcium events globally involved the entire tuft tree, consistent with previous reports in visual, anterior lateral motor (ALM), and somatosensory cortices (8–11). The differences in the structure-function correlations between type 1 and type 2 PTNs were not related to the cluster subdivision. They were also evident when the analysis was performed on the whole event population (Fig. 3,

L to P). However, in type 1 PTNs, the subdivision into the four clusters highlighted more details because using the entire population averaged events with different spatial activation patterns.

Plotting Mantel statistics as a function of nexus size for individual neurons, we found a clear distinction between the two PTN subclasses despite the variability in size within both groups Support Vector Machine (SVM) accuracy 1,

chance 0.52 for both clusters). This finding further strengthens the anatomical subdivision based on independent physiological parameters (fig. S7F).

We next investigated the relationship between tuft tree and somatic activation using quasi-simultaneous imaging of tuft and soma (~10-Hz acquisition rate). For type 1 PTNs, we observed that events encompassing the full tuft or restricted to an entire hemi-tree were invariantly associated with somatic activation in all (100%) events examined. For events encompassing only part of a hemi-tree, somatic activation was proportional to the percentage of active ROIs (Fig. 4, A to D). In type 2 PTNs, somatic activation was proportional to the extent of ROI recruitment in the entire tree (Fig. 4, E and F). The tuft activity was critically dependent on NMDA receptor (NMDAR) channels because local injection of the NMDAR blocker MK801 close to the imaged tuft blocked both tuft and somatic activity (fig. S8).

Next, we investigated the possible functional importance of tuft compartmentalization. For both type 1 and type 2 PTNs, the activity in tuft dendrites strongly correlated with motor behavior (fig. S9). To evaluate the preferential selectivity of responses for specific behavioral variables in the different tuft dendrites in individual neurons, we modeled the calcium transients using a generalized linear model (GLM) (Fig. 5 and fig. S10A; see materials and methods) (34, 41, 42). For both type 1 and type 2 layer 5 PTNs, the activity in tuft dendrites was strongly related to individual motor variables. The GLM effectively modeled the calcium activity of both hand reach and running on treadmill behavioral events (Fig. 5). On average, for type 1 and type 2 PTNs, the full GLM successfully modeled the ROIs activity, achieving explained variance >0.15 in 77.5 and 63.8% of ROIs for the hand reach task and 56.5 and 73% of ROIs for the treadmill task, respectively (Fig. 5U).

For type 1 PTNs, representation was not uniform throughout the tuft for either hand reach or treadmill behaviors. We observed a differential representation of motor variables in the different tuft tree segments (Fig. 5, A to J and V to W, and fig. S10B). The largest nonuniformity was typically observed between the R/L tuft hemi-trees with different combinations of motor variables preferentially encoded by each of the two hemi-trees activity (Fig. 5, A to J, and fig. S10B). However, we also could observe dendrites within each hemi-tree, which were tuned to different combinations of motor variables (fig. S10B). To quantify the spatial compartmentalization of motor variables representation within and between the hemi-trees of single type 1 PTNs, we performed pairwise Pearson correlations between the GLM selectivity vectors of the dif-

ferent ROIs (Fig. 5, D, E, I, and J, and fig. S10B). Overall, type 1 PTNs demonstrated a correlation between the pairwise Pearson correlation coefficient of the GLM selectivity vectors and the distance between ROIs (Fig. 5, A to J and V). Consistently, we observed a significant correlation between the tuft distance matrix and GLM vector matrix for both behavioral data (Fig. 5, V and W). The significance of R/L segregation was further examined by comparing our experimental Pearson correlations between R/L hemi-trees to randomly distributed ROIs (1000 permutations). Experimental Pearson values between R/L hemi-trees were significantly smaller compared with the permuted values (Z-scores of -2.94 ± 2.6 ; p values were <0.05 in 80% of cases). Moreover, when we plotted the Pearson correlation matrices of peri-behavioral event time segments for different behavioral events, we found marked differences in the dendritic compartmentalization between different behavioral events for both tasks (fig. S11), further indicating differential spatial dendritic representation of various motor events.

By contrast, GLM analysis for type 2 PTNs revealed a more uniform encoding of motor variables along the tuft and only minimal correlation to the tuft tree structure (Fig. 5, K to T). Although the GLM vectors for the different ROIs of the same single neuron were not completely identical, we did not observe systematic differences between or within the hemi-trees (Fig. 5, V and W; comparison of experimental and permuted random ROI locations yielded Z-scores of -0.47 ± 1.72 ; p values were <0.05 in 27% of cases; $p < 0.01$ comparing between Z-scores of type 1 and type 2 PTNs, Wilcoxon rank test).

To understand the impact of the differential tuft activity on the output of type 1 and type 2 PTNs, we performed tuft and soma imaging from the same neurons. We hypothesized that the combined computational products of the hemi-trees will affect the representation of motor variables at the soma. Indeed, GLM modeling of the somatic activity revealed a composite tuning that reflected the summed representation of both hemi-trees for type 1 and 2 PTNs (Fig. 5, B and L, and fig. S12). We found high Pearson correlation coefficients between the GLM vectors of the R/L tuft ROIs and the corresponding somas for type 1 and even more so for type 2 PTNs (Fig. 5X).

To further investigate the mechanisms underlying the observed activity in vivo, we performed modeling experiments on reconstructed type 1 and type 2 PTNs using the neuron platform (Fig. 6). We activated the tuft tree with pseudorandom patterned inputs (Fig. 6, A to C) and in vivo-like activation frequencies (43, 44). Compatible with our in vivo results, we could readily observe

R/L hemi-tree separation and compartmental calcium responses within hemi-tree tuft branches in a type 1 (Fig. 6C; compare Fig. 6D and Fig. 2, C to E, and movies S7 to S10; same neuron as in Fig. 2, A to E) but not in type 2 PTNs (fig. S13; same neuron as in Fig. 3, A to C). However, the in vivo results showed a higher intercorrelation within terminal subtrees for clusters 2 and 3 events, probably reflecting a nonrandom input distribution on the tuft tree in vivo (fig. S14, A and B). The simulated voltage correlation matrices also captured the main features of the tuft tree segmentation (Fig. 6F). Yet, the voltage signals showed higher correlations than the calcium signals, reflecting the localized calcium influx to the synaptic sites (via NMDAR) and the high-pass filtering effect of voltage-gated calcium channels (VGCCs) [see also Lavzin *et al.* (45)].

Next, we used our simulations to characterize the nature of the calcium event clusters. In type 1 PTNs, the four clusters differed primarily in the degree of recruitment of the NMDAR spiking mechanism (Fig. 6E). In type 2 PTNs, massive and widespread recruitment of NMDA spikes already occurred in cluster 2 events (fig. S13, D and H). Consistent with the critical role of NMDAR spiking mechanisms in replicating the in vivo findings, simulations with AMPAR-only synapses (Fig. 6B) failed to generate significant tuft activation (46). These results agree with our experimental demonstration of a marked reduction in the calcium activity of tuft dendrites after NMDAR blockade (fig. S8). We then investigated the contribution of VGCCs to tuft compartmentalization in type 1 PTNs. Elimination of VGCCs from the nexus had little impact on tuft segmentation, except for cluster 4 events, where removal of VGCCs increased R/L hemi-tree segmentation (Fig. 6G). Taken together, our simulations show that tuft segmentation is primarily dependent on differential recruitment of NMDAR spiking mechanisms in different tuft branches, and VGCCs play a minimal role in this process.

Because we could replicate the major characteristics of our experimental results with pseudo-random input patterns in both type 1 and 2 PTNs, we hypothesized that the distinct degrees of tuft segmentation must be linked to the difference in dendritic morphology, especially nexus size. To investigate this hypothesis, we scaled down the size of the apical arbor of the type 1 PTN but kept the soma-tuft distance unchanged. Under these conditions, we observed a sharp reduction in the segmentation within and between the hemi-trees (Fig. 6, H and I). This conclusion is further supported by our voltage simulations, which show that dendritic independence was primarily driven by the sizable electrotonic distance along the nexus (fig. S14C) and by the decreased NMDAR-dependent nonlinear interactions as a function

of the distance between dendritic locations, with only minimal interactions between the two hemi-trees [fig. S14D; see also Kerlin *et al.* (11)].

Discussion

Overall, our results reveal a subclass of thick-tufted layer 5 PTNs in M1 (type 1) that performs parallel independent representations of motor information within its tuft dendrites. The degree of tuft compartmentalization was primarily dependent on the nexus and tuft tree morphology and required the NMDA spiking mechanism. In these neurons, motor information is integrated and amplified via NMDA spikes within adjustable segments of the tuft, ranging from small tertiary and quarterly sister branches, independent R/L hemi-trees, and up to a single global computational compartment in the minority of events. Our modeling suggests that calcium spikes play only a minimal role in tuft compartmentalization and local amplification. Instead, the initiation of calcium spikes in the distal apical trunk and proximal nexus branches probably serves to further amplify the tuft computational products (46, 47).

Type 2 PTNs also amplify behaviorally relevant motor information within their tuft but in a more global manner, mostly functioning as a single computational compartment (8–11).

The type 1 subclass constitutes a sizable fraction of thick-tufted layer 5 PTNs (~40%), in line with previous reports (24, 26). Although we based our classification solely on the apical dendritic morphology, our physiological findings supported this classification. Studies that examined both dendritic morphology and projection targets suggest that type 1 PTNs may preferentially project to the medulla (23, 27, 32), which is consistent with our medulla and spinal cord retrograde-labeled PTNs. Further studies are required to examine the projection pattern and molecular markers of type 1 and 2 PTNs (23, 32).

Our results reconcile the differences in the findings of prior *in vitro* and modeling studies, which predicted the capacity of dendrites to compartmentalize information (4, 17, 22, 48, 49) and recent recordings from behaving mice, which show that tuft dendrites function primarily as a single global amplification unit (8–11). Several past studies also observed infrequent local spikes that were limited to small, non-overlapping dendritic segments in tuft dendrites (9–11). Yet, this highly localized spiking activity, reminiscent of our cluster 1 events, cannot serve for efficiently communicating tuft computations to the soma. It may be used for local plasticity instead (6, 27). A study (6) that recorded tuft dendrites of M1 layer 5 PTNs reported spatially isolated dendritic spikes in almost all pairs of sibling distal tuft branches (95%). The results of this study dif-

fer from ours, as we observed selective activation of sibling terminal tuft branches during both motor tasks infrequently (<5%). These results are especially surprising in the case of type 2 layer 5 PTNs, which should have also been observed in that study. The discrepancies between our findings and those of (6) were probably related technical issues such as the low acquisition rate and the lack of adequate sparse labeling in (6).

The R/L hemi-tree compartmentalization is perhaps one of the most distinctive and intriguing properties of type 1 PTNs, which was not anticipated from previous work. This hemi-tree tuft compartmentalization enables PTNs to represent different sets of information in parallel, with each hemi-tree routing information to the soma independently acting as “a neuron within a neuron.” It is conceivable that in larger and more complex primate and human PTNs, this property would have an even larger impact, with a greater number of almost isolated integrative zones in the tuft (50, 51).

On the basis of our data, we propose a new integration and representation scheme of motor variables in tuft dendrites of M1 layer 5 PTNs. Motor variables are not represented in fully compartmentalized, small, nonoverlapping dendritic segments as previously reported (6). Instead, a given motor behavior or a sequence is represented by the activation of a specific combination of distal tuft segments, which are mutually coamplified via NMDA spikes to form spatial dendritic amplification maps for different motor behaviors. In this framework, the tuft tree of type 1 layer 5 PTNs is capable of dynamic combinatorial representation of a large number of motor variables and sequences within the same dendritic tuft branches (2, 52, 53).

REFERENCES AND NOTES

- T. Branco, M. Häusser, *Curr. Opin. Neurobiol.* **20**, 494–502 (2010).
- X. E. Wu, B. W. Mel, *Neuron* **62**, 31–41 (2009).
- G. J. Stuart, N. Spruston, *Nat. Neurosci.* **18**, 1713–1721 (2015).
- G. Major, M. E. Larkum, J. Schiller, *Annu. Rev. Neurosci.* **36**, 1–24 (2013).
- S. D. Antic, W. L. Zhou, A. R. Moore, S. M. Short, K. D. Ikonou, *J. Neurosci. Res.* **88**, 2991–3001 (2010).
- J. Cichon, W. B. Gan, *Nature* **520**, 180–185 (2015).
- L. M. Palmer *et al.*, *Nat. Neurosci.* **17**, 383–390 (2014).
- L. Beaulieu-Laroche, E. H. S. Toloza, N. J. Brown, M. T. Harnett, *Neuron* **103**, 235–241.e4 (2019).
- V. Francioni, Z. Padamsey, N. L. Rochefort, *eLife* **8**, e49145 (2019).
- J. Voigts, M. T. Harnett, *Neuron* **105**, 237–245.e4 (2020).
- A. Kerlin *et al.*, *eLife* **8**, e46966 (2019).
- N. L. Xu *et al.*, *Nature* **492**, 247–251 (2012).
- C. O. Lacefield, E. A. Pnevmatikakis, L. Paninski, R. M. Bruno, *Cell Rep.* **26**, 2000–2008.e2 (2019).
- B. B. Ujfalussy, J. K. Makara, M. Lengyel, T. Branco, *Neuron* **100**, 579–592.e5 (2018).
- R. Naud, B. Bathellier, W. Gerstner, *Front. Comput. Neurosci.* **8**, 90 (2014).
- P. Poirazi, T. Brannon, B. W. Mel, *Neuron* **37**, 989–999 (2003).
- D. Beniaguev, I. Segev, M. London, *Neuron* **109**, 2727–2739.e3 (2021).
- A. Payeur, J. C. Béique, R. Naud, *Curr. Opin. Neurobiol.* **58**, 78–85 (2019).
- G. Kastellakis, P. Poirazi, *Front. Mol. Neurosci.* **12**, 300 (2019).
- R. Legenstein, W. Maass, *J. Neurosci.* **31**, 10787–10802 (2011).
- J. Bono, C. Clopah, *Nat. Commun.* **8**, 706 (2017).
- B. W. Mel, in *Advances in Neural Information Processing Systems*, J. Moody, S. Hanson, R. Lippmann, Eds. (Morgan Kaufmann, 1992), vol. 4, pp. 35–42.
- M. N. Economo *et al.*, *Nature* **563**, 79–84 (2018).
- H. Markram *et al.*, *Cell* **163**, 456–492 (2015).
- W. J. Gao, Z. H. Zheng, *J. Comp. Neurol.* **476**, 174–185 (2004).
- Y. Wang, M. Ye, X. Kuang, Y. Li, S. Hu, *IBRO Rep.* **5**, 74–90 (2018).
- S. Jiang *et al.*, *Sci. Rep.* **10**, 7916 (2020).
- G. M. Shepherd, *Nat. Rev. Neurosci.* **14**, 278–291 (2013).
- A. Groh *et al.*, *Cereb. Cortex* **20**, 826–836 (2010).
- E. J. Kim, A. L. Juavinett, E. M. Kyubwa, M. W. Jacobs, E. M. Callaway, *Neuron* **88**, 1253–1267 (2015).
- A. M. Hattox, S. B. Nelson, *J. Neurophysiol.* **98**, 3330–3340 (2007).
- B. Tasic *et al.*, *Nature* **563**, 72–78 (2018).
- L. N. Fletcher, S. R. Williams, *Neuron* **101**, 76–90.e4 (2019).
- S. Levy *et al.*, *Neuron* **107**, 954–971.e9 (2020).
- F. Fuhrmann *et al.*, *Neuron* **86**, 1253–1264 (2015).
- T. W. Chen *et al.*, *Nature* **499**, 295–300 (2013).
- T. Deneux *et al.*, *Nat. Commun.* **7**, 12190 (2016).
- N. Mantel, *Cancer Res.* **27**, 209–220 (1967).
- B. Manly, *The Statistics of Natural Selection* (Chapman & Hall, 1985).
- P. W. Mielke, *Biometrics* **34**, 277 (1978).
- B. Engelhard *et al.*, *Nature* **570**, 509–513 (2019).
- P. Ramkumar, B. Dekleva, S. Cooler, L. Miller, K. Kording, *PLOS ONE* **11**, e0160851 (2016).
- B. A. Sauerbrei *et al.*, *Nature* **577**, 386–391 (2020).
- A. Nashev, O. Cohen, R. Harel, Z. Israel, Y. Prut, *Cell Rep.* **27**, 2608–2619.e4 (2019).
- M. Lavzin, S. Rapoport, A. Polksy, L. Garion, J. Schiller, *Nature* **490**, 397–401 (2012).
- M. E. Larkum, T. Nevian, M. Sandler, A. Polksy, J. Schiller, *Science* **325**, 756–760 (2009).
- M. Larkum, *Trends Neurosci.* **36**, 141–151 (2013).
- H. Jia, N. L. Rochefort, X. Chen, A. Konnerth, *Nature* **464**, 1307–1312 (2010).
- M. E. Sheffield, D. A. Dombeck, *Nature* **517**, 200–204 (2015).
- L. Beaulieu-Laroche *et al.*, *Cell* **175**, 643–651.e14 (2018).
- H. Mohan *et al.*, *Cereb. Cortex* **25**, 4839–4853 (2015).
- R. Urbanczki, W. Senn, *Neuron* **81**, 521–528 (2014).
- J. Hawkins, S. Ahmad, *Front. Neural Circuits* **10**, 23 (2016).

ACKNOWLEDGMENTS

We thank S. Marom and B. Engelhard for helpful comments on the manuscript. We also thank S. Schwartz for advice in statistical tests and S. Gafniel for movie editing. **Funding:** This study was partially supported by the Israeli Science Foundation (J.S. and Y.S.), Prince funds (J.S. and Y.S.), Rappaport Foundation (J.S. and Y.S.), and Zuckerman Postdoctoral Fellowship (N.C.).

Author contributions: Designed research: J.S., N.C., Y.S.

Performed experiments: Y.O., N.C., S.A., M.A. Analyzed data: S.A., Y.O., J.S., H.B., O.B., Y.S. Writing – original draft: J.S.

Writing – review and editing: J.S., Y.O., S.A., A.P.-P., Y.S.

Performed simulations: A.P.-P., S.A., J.S. **Competing interests:**

The authors declare that they have no competing interests. **Data and materials availability:** All data are available in the manuscript or the supplementary materials. Computer code can be found in: <https://github.com/SchillersLab/Dynamic-compartmental-computations-in-tuft-dendrites->.

SUPPLEMENTARY MATERIALS

science.org/doi/10.1126/science.abn1421

Materials and Methods

Figs. S1 to S14

References (54–60)

MDAR Reproducibility Checklist

Movies S1 to S10

[View/request a protocol for this paper from Bio-protocol.](https://www.bio-protocol.org/submit-a-protocol)

7 November 2021; accepted 11 March 2022

10.1126/science.abn1421